ORIGINAL PAPER

Nonlinear dynamic analysis of supercritical and subcritical Hopf bifurcations in gas foil bearing-rotor systems

Runeng Zhou · Yongpeng Gu · Jiang Cui · Gexue Ren · Suyuan Yu

Abstract The Hopf bifurcation behavior is an important issue for the nonlinear dynamic analysis of gas foil bearing (GFB)-rotor systems. However, there is a lack of detailed study on different types of Hopf bifurcation and their corresponding characteristics for GFB-rotor systems. This paper is intended to provide a clear and systematic insight into the nonlinear dynamic characteristics of GFB-rotor systems with a supercritical or a subcritical Hopf bifurcation. The onset speed (OS) of instability (i.e., the bifurcation point) for the system is calculated by the linear stability analysis. The periodic solution of the system before or after the bifurcation point is obtained by the shooting method, and its stability is assessed by the Floquet multipliers. The shock stability and the unbalanced response characteristics of the GFB-rotor system with a supercritical or a subcritical Hopf bifurcation are presented. A GFB-rotor system with a supercritical Hopf bifurcation shows better dynamic characteristics than a system with a subcritical Hopf bifurcation. The parameter analysis reveals that the aspect ratio and the foil stiffness of the GFBs have obvious effects on the Hopf bifurcation type, while the loss factor has a relatively small effect. It is remarkable that although a lower foil stiffness increases the OS of instability, the actual speed limit would probably decrease as the Hopf bifurcation changes from a supercritical to a subcritical type. This can contribute to an understanding of the necessity of studies on actual available operating speed based on nonlinear analysis rather than conventional linear analysis for the bearing design.

R. Zhou · S. Yu
Department of Energy and Power Engineering, Tsinghua University, Beijing 100084, China
e-mail: zhourn19@mails.tsinghua.edu.cn

S. Yu
e-mail: suyuan@tsinghua.edu.cn

Y. Gu (✉)· J. Cui · G. Ren
School of Aerospace Engineering, Tsinghua University, Beijing 100084, China
e-mail: guyp@tsinghua.edu.cn

J. Cui
e-mail: cuij17@mails.tsinghua.edu.cn

G. Ren
e-mail: rengx@tsinghua.edu.cn

1 Introduction

Gas foil bearings (GFBs) are self-acting gas-lubricated bearings with a compliant foil structure. In comparison with conventional rolling element and oil-lubricated bearings, GFBs have significant advantages such as fewer components, the elimination of oil, lower frictional losses, and wider operational temperature ranges [1,2]. Therefore, GFBs are increasingly employed in advanced high-speed, high-performance, and long-life rotating machinery systems. Among the various types of GFBs, the bump-type foil bearing is the most widely

studied and used [3]. However, due to the low viscosity of the gas, the damping capacity of GFBs is fairly limited, which may result in nonlinear vibrations or instability under high-speed conditions [4]. The stability and vibration problems are still key issues for their application in high-speed rotors, and many efforts have been made to study the stability and vibration characteristics of GFB-rotor systems using linear and nonlinear dynamic analysis.

The early studies of the dynamics for GFB-rotor systems relied on linear dynamic analysis, due to the limited computer power and numerical techniques available at that time. In most of these linear analyses, the force coefficient (FC) method that was first introduced by Lund [5] was used to represent the gas film forces. Peng and Carpino [6] proposed a calculation method for the FC of GFBs. Based on this FC method, the characteristics of the onset speed (OS) of instability were widely investigated in [7–10]. Vleugels et al. [7] demonstrated that a foil structure with a proper design could increase the OS of instability. In recent years, the accuracy of the FC method for compliant gas bearings has been discussed and improved in [11–13]. Besides, it has been demonstrated that the stability of the static equilibrium point can be assessed directly based on an eigenvalue analysis [14].

Nevertheless, it is far from enough to just perform the linear analysis of GFB-rotor systems. Due to the nonlinear hydrodynamic film, experiments and simulations of the rotors supported on the bump-type GFBs show significant subsynchronous vibrations and frequency-locking behaviors [4,9,10,15–19]. Similar subsynchronous vibration phenomena were also widely observed in rotor systems supported by other types of gas bearings [20–28]. The first study to attempt to explain the nonlinear vibrations was presented by San Andrés and Kim [15] using a reduced numerical model that neglected the gas film under the assumption of a very stiff gas film. They suggested the cause of the subsynchronous vibrations as a forced nonlinearity under high unbalanced levels rather than typical hydrodynamic bearing instability. Inspired by the work of Andrés and Kim [15], Hoffmann et al. [9] investigated the effect of the nonlinear fluid film forces on the subsynchronous vibrations and found that the system may be self-excited by the gas film forces with a frequency related to the system's natural frequency. Their results also indicated that the speed range of the subsynchronous vibrations, which characterize stable

Hopf bifurcation behavior, decreases and finally disappears with the increase in the static load. A coincident conclusion could be drawn from the simulation results of Gu et al. [29] in which no subsynchronous vibrations existed before the film failure. A more systematic investigation was conducted by Hoffmann and Liebich [10] experimentally and numerically. The two causes of subsynchronous vibrations were studied individually, and one of the findings was that a higher unbalanced value would result in a lower onset speed of subsynchronous vibrations.

Except for the subsynchronous vibrations, another noteworthy nonlinear topic is the existence of stable and unstable periodic solutions (i.e., limit cycles). On the one hand, Pham and Bonello [30] noticed that there was no stable limit cycle in a GFB-rotor system with the most commonly used parameters, while a stable limit cycle was obtained with a very stiff foil structure and a small bearing clearance. Bonello and Pham [31] gave a specific explanation that attributed this to the compliance of the foil structure, in view of the fact that limit cycles have been numerically obtained in rotors supported by rigid gas bearings in [20,22]. On the other hand, an unstable limit cycle was found by Yang et al. [32] in rigid gas bearings, which results in a shock instability phenomenon; in other words, the nonlinear stability of the system is determined by the amplitude of the disturbance.

In fact, the disagreements about the existence of subsynchronous vibrations and stable or unstable periodic solutions come from different Hopf bifurcation behaviors (i.e., supercritical Hopf bifurcation and subcritical Hopf bifurcation) [33]. The investigations of different Hopf bifurcation behaviors are very common in oil journal bearings [34–38]. Although most of them were based on analytical formulas for an infinitely long or an infinitely short journal bearing, the investigation carried out by Chasalevris [38] greatly highlighted the significance of the prediction of the Hopf bifurcation behaviors and the actual available speed range in oil journal bearing-rotor systems. However, the commonly used methods applied in these works are not suitable for gas bearing systems, because no analytical formulas are feasible to describe the dynamic gas film forces. Furthermore, due to the compressibility of the gas film and the introduction of a complaint foil structure, a GFB-rotor system is a multi-field coupling system with a large number of degrees of freedom, while the analytical method applied in oil journal bearings to character-

ize the stability of periodic solutions makes sense only in systems with few degrees of freedom [38]. Therefore, a different approach is needed to characterize the Hopf bifurcation behaviors in GFB-rotor systems.

The Hopf bifurcation behaviors are vitally important in the nonlinear dynamic analysis of GFB-rotor systems, because different Hopf bifurcation behaviors lead to entirely different nonlinear dynamic characteristics of the system. It is worth noting that the subcritical Hopf bifurcation is often potentially dangerous in engineering applications, which has been widely concerned. However, to the knowledge of the authors, no research related to different Hopf bifurcation types, especially the subcritical Hopf bifurcation, has been reported in the field of gas bearing. In order to fill the gap in the research on different Hopf bifurcation behaviors in GFB-rotor systems, the nonlinear dynamic characteristics of GFB-rotor systems with a supercritical Hopf bifurcation or a subcritical Hopf bifurcation are investigated in this paper. The periodic solution of the system is obtained by the shooting method, and its stability is assessed by Floquet multipliers. The analysis results provide a clear and systematic insight into the nonlinear dynamic characteristics of the two typical Hopf bifurcation behaviors, which are fragmentarily reflected in previous studies. The parameter analysis provides guidance for the design of GFBs to achieve high actual available operating speed based on nonlinear analysis rather than the conventional high OS of instability based on linear analysis.

2 Governing equations and solutions

The present work is based on a classical GFB-rotor system, as shown in Fig. 1. The center of the fixed bearing sleeve is chosen as the origin of the Cartesian coordinates. The x, y, and z axes are defined to point in the vertical direction, the horizontal direction, and the axial direction of the bearing, respectively. The unbalance is assumed to be located on the center disk only; hence, the responses of both bearings are constrained to be identical, and the system is modeled as a point-mass rotor in a GFB.

In order to obtain the dimensionless governing equations of the system, four characteristic variables are used: the radial clearance C as the characteristic length in the x and y directions, the bearing radius R as the characteristic length in the angular and axial directions of the bearing, the inverse of the rotational speed $1/\Omega$
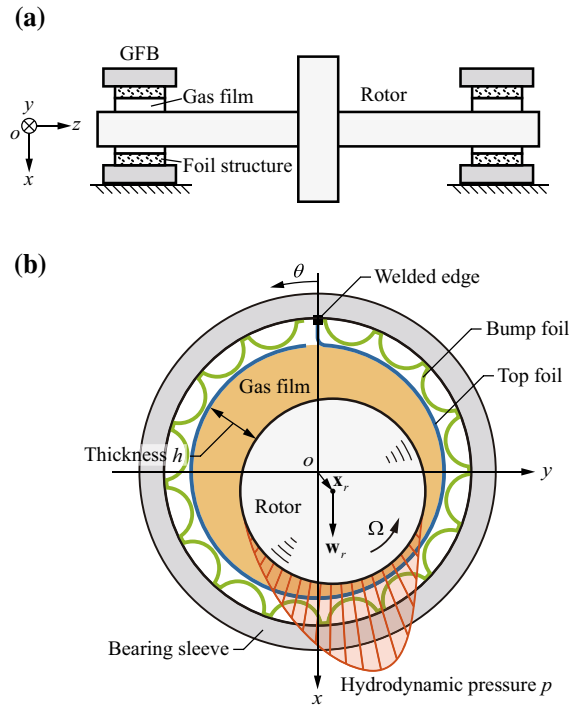
Fig. 1 A symmetric GFB-rigid rotor system: **a** the configuration of the system and **b** the schematic of a bump-type GFB with associated nomenclature

as the characteristic time, and the ambient pressure p_a as the characteristic pressure. Then, the dimensionless pressure $\tilde{p}$, time τ, mass $\tilde{m}$, and force vector $\tilde{\mathbf{f}}$ can be written as:

$$\tilde{p} = \frac{p}{p_a}, \ \tau = \Omega t, \ \tilde{m} = \frac{\Omega^2 C}{p_a R^2} m, \ \tilde{\mathbf{f}} = \frac{\mathbf{f}}{p_a R^2} \qquad (1)$$

2.1 Analytical model

Given $\tilde{\mathbf{x}}_r = \begin{bmatrix} e_x, e_y \end{bmatrix}^{\mathrm{T}}$ as the dimensionless displacement of the rigid rotor, the dimensionless equation governing the motion of the rigid rotor is

$$\ddot{\tilde{\mathbf{x}}}_r = \frac{1}{\tilde{m}_r} \left(\tilde{\mathbf{w}}_r + \tilde{\mathbf{f}}_p + \tilde{\mathbf{f}}_{ub} \right) \qquad (2)$$

where $\tilde{m}_r$ is the dimensionless rotor mass, and $\tilde{\mathbf{w}}_r = \begin{bmatrix} \tilde{w}_r, 0 \end{bmatrix}^{\mathrm{T}}$ is the dimensionless static load vector. The dimensionless gas film force vector $\tilde{\mathbf{f}}_p$ is obtained by integrating the film pressure distribution over the whole bearing surface, as follows:

$$\tilde{\mathbf{f}}_p = \int_{-L/2R}^{L/2R} \int_0^{2\pi} (\tilde{p} - 1) \, \mathbf{A}_\theta \mathrm{d}\theta \mathrm{d}\zeta \qquad (3)$$

where $\theta \in [0, 2\pi]$ is the angular coordinate along the rotational direction of the rotor, and $\zeta = z/R \in [-L/2R, L/2R]$ is the dimensionless Cartesian coordinate along the axial direction of the bearing, L is the bearing length, and $\mathbf{A}_\theta = [\cos\theta, \sin\theta]^{\mathrm{T}}$. The Gümbel condition is adopted to make a correction for the subambient pressure; in other words, the contribution of $\tilde{p} < 1$ is omitted in integration (3). The dimensionless unbalanced force vector $\tilde{\mathbf{f}}_{ub}$ is

$$\tilde{\mathbf{f}}_{ub} = \frac{u\Omega^2}{p_a R^2} \begin{bmatrix} \cos(\tau + \theta_0) \\ \sin(\tau + \theta_0) \end{bmatrix} \tag{4}$$

where u is the unbalance, and θ_0 is the initial phase of the unbalanced force.

The gas flow in the bearing is assumed to be a laminar, Newtonian, and compressible thin-film flow under isothermal condition. Hence, the dimensionless gas film pressure $\tilde{p}(\theta, \zeta)$ is governed by the Reynolds equation for an isothermal compressible perfect fluid [39]. The dimensionless form of the Reynolds equation is written as:

$$2S\frac{\partial}{\partial\tau}\left(\tilde{p}\tilde{h}\right) + S\frac{\partial}{\partial\theta}\left(\tilde{p}\tilde{h}\right)$$
$$= \frac{\partial}{\partial\theta}\left(\tilde{p}\tilde{h}^3\frac{\partial\tilde{p}}{\partial\theta}\right) + \frac{\partial}{\partial\zeta}\left(\tilde{p}\tilde{h}^3\frac{\partial\tilde{p}}{\partial\zeta}\right) \tag{5}$$

where $S = 6\mu\Omega/p_a (R/C)^2$ is the bearing number, μ the dynamic viscosity of the gas, and $\tilde{h} = h/C$ the dimensionless film thickness. By introducing a variable $\psi = \tilde{p}\tilde{h}$, the Reynolds Eq. (5) is transformed into the following equation:

$$\frac{\partial\psi}{\partial\tau} = \frac{1}{2S}\left\{\frac{\partial}{\partial\theta}\left[\psi\left(\tilde{h}\frac{\partial\psi}{\partial\theta} - \psi\frac{\partial\tilde{h}}{\partial\theta}\right)\right]\right.$$
$$\left. + \frac{\partial}{\partial\zeta}\left[\psi\left(\tilde{h}\frac{\partial\psi}{\partial\zeta} - \psi\frac{\partial\tilde{h}}{\partial\zeta}\right)\right]\right\} - \frac{1}{2}\frac{\partial\psi}{\partial\theta} \tag{6}$$

The dimensionless film thickness is expressed as:

$$\tilde{h} = 1 + e_x\cos\theta + e_y\sin\theta + \tilde{w} \tag{7}$$

where $\tilde{w} = w/C$ is the dimensionless foil deflection.

The gas film is open to the environment on all sides; hence, the pressure at each edge is constant and is set as the ambient pressure p_a; in other words, $\tilde{p} = 1$. For Eq. (6) with $\psi = \tilde{p}\tilde{h}$, the boundary condition is that $\psi = \tilde{h}$ at the bearing edges.

The simple elastic foundation model is introduced to model the foil structure, considering its good correlation with the experimental results and high efficiency for dynamic simulations [40,41]. This is a damped Winkler foundation model with a stiffness per unit area, k_b, and an equivalent viscous damping coefficient, c_b. The hysteretic damping is used to model the energy dissipation of the foil structure; in other words, $c_b = \eta_f k_b/\omega_f$, where η_f is the mechanical loss factor of the bump foil, and ω_f is the oscillation frequency. The time domain analysis needs to fix the oscillation frequency ω_f at a certain value, and the most commonly used method is to set ω_f as the rotational speed Ω. Besides, the assumption of a constant foil deflection in the axial direction is much more coincident with the real situations for the first-generation GFBs. The dimensionless equation governing the deflection of the foil structure can be written as:

$$\dot{\tilde{w}}(\theta) = \frac{1}{\eta_f}\left(\frac{\tilde{P}_\theta(\theta)}{\tilde{k}_b^\theta} - \tilde{w}(\theta)\right) \tag{8}$$

where $\tilde{k}_b^\theta = k_b C/p_a$ is the dimensionless form of k_b, and $\tilde{P}_\theta(\theta) = R/L \int_{-L/2R}^{L/2R}(\tilde{p}(\theta, \zeta) - 1)\,\mathrm{d}\zeta$ is the average dimensionless gauge pressure over the axial direction.

Finally, the GFB-rotor system is governed by Eqs. (2), (6), and (8).

2.2 Discretization

As the Reynolds equation is a nonlinear partial differential equation, to obtain the dynamic responses of the GFB-rotor system established in Sect. 2.1, the help of numerical methods is needed. The finite difference method is used to discretize the equations in the spatial field. By so doing, the governing equations of the entire system are discretized into a set of ordinary differential equations (ODEs); thus, the nonlinear transient analysis can be performed by using a numerical integration algorithm.

The gas film domain is meshed into a uniform rectangular grid with $N_\theta \times N_\zeta$ points, in which N_θ and N_ζ are the number of points along the angular and axial directions of the bearing, respectively. The continuous variables ψ and $\tilde{w}$ are replaced by the discrete approximations $\psi_{i,j}$ and $\tilde{w}_i$ where $i = 1, \ldots, N_\theta$ and

$j = 1, \ldots, N_\zeta$. Using a central difference scheme, the partial derivatives in Eq. (6) can be approximated as:

$$\left.\frac{\partial \psi}{\partial \theta}\right|_{i,j} \approx \frac{\psi_{i+1,j} - \psi_{i-1,j}}{2\Delta\theta},$$

$$\left.\frac{\partial^2 \psi}{\partial \theta^2}\right|_{i,j} \approx \frac{\psi_{i+1,j} - 2\psi_{i,j} + \psi_{i-1,j}}{(\Delta\theta)^2},$$

$$\left.\frac{\partial \psi}{\partial \zeta}\right|_{i,j} \approx \frac{\psi_{i,j+1} - \psi_{i,j-1}}{2\Delta\zeta},$$

$$\left.\frac{\partial^2 \psi}{\partial \zeta^2}\right|_{i,j} \approx \frac{\psi_{i,j+1} - 2\psi_{i,j} + \psi_{i,j-1}}{(\Delta\zeta)^2},$$

$$\left.\frac{\partial \tilde{h}}{\partial \theta}\right|_{i,j} \approx [-\sin\theta, \cos\theta]\,\tilde{\mathbf{x}}_r$$
$$+ \frac{\tilde{w}_{i+1} - \tilde{w}_{i-1}}{2\Delta\theta},$$

$$\left.\frac{\partial^2 \tilde{h}}{\partial \theta^2}\right|_{i,j} \approx [-\cos\theta, -\sin\theta]\,\tilde{\mathbf{x}}_r$$
$$+ \frac{\tilde{w}_{i+1} - 2\tilde{w}_i + \tilde{w}_{i-1}}{(\Delta\theta)^2},$$

$$\left.\frac{\partial \tilde{h}}{\partial \zeta}\right|_{i,j} = 0, \quad \left.\frac{\partial^2 \tilde{h}}{\partial \zeta^2}\right|_{i,j} = 0 \tag{9}$$

for the interior grid points ($i = 2, \ldots, N_\theta - 1$ and $j = 2, \ldots, N_\zeta - 1$). $\Delta\theta$ and $\Delta\zeta$ refer to the step sizes in the respective directions. The boundary conditions are implemented by applying $\psi_{i,j} = \tilde{h}_i$ on the boundary points ($i = 1, N_\theta$ or $j = 1, N_\zeta$).

With the approximated partial derivatives, the governing equation of $\psi_{i,j}$ can be discretized as a nonlinear ODE:

$$\dot{\psi}_{i,j} = g_{i,j}(\tilde{\mathbf{x}}_r, \psi_{i,j}, \psi_{i-1,j}, \psi_{i,j-1},$$
$$\psi_{i+1,j}, \psi_{i,j+1}, \tilde{w}_{i-1}, \tilde{w}_i, \tilde{w}_{i+1}) \tag{10}$$

For the foil structure, the governing equation is discretized as:

$$\dot{\tilde{w}}_i = \frac{1}{\eta_f}\left(\frac{\tilde{P}_{\theta,i}}{\tilde{k}_b^\theta} - \tilde{w}_i\right) \tag{11}$$

where the average dimensionless gauge pressure over the axial direction is expressed as:

$$\tilde{P}_{\theta,i} = R/L \int_{-L/2R}^{L/2R} \left(\frac{\psi(\theta_i, \zeta)}{\tilde{h}(\theta_i)} - 1\right) d\zeta$$
$$\approx \frac{1}{N_\zeta - 1}\left(1 + \sum_{j=2}^{N_\zeta - 1} \frac{\psi_{i,j}}{\tilde{h}_i}\right) - 1 \tag{12}$$

Similarly, the discrete expression of the dimensionless gas film force vector $\tilde{\mathbf{f}}_p$ is

$$\tilde{\mathbf{f}}_p = \int_{-L/2R}^{L/2R} \int_0^{2\pi} \left(\frac{\psi}{\tilde{h}} - 1\right) \mathbf{A}_\theta d\theta d\zeta \approx$$
$$\Delta\theta\Delta\zeta \sum_{i=2}^{N_\theta - 1} \sum_{j=2}^{N_\zeta - 1} \left[\left(\frac{\psi_{i,j}}{\tilde{h}_i} - 1\right)\mathbf{A}_{\theta_i}\right] \tag{13}$$

After the discretization, the governing equations of the system can be written as:

$$\begin{cases} \ddot{\tilde{\mathbf{x}}}_r = \frac{1}{\tilde{m}_r}\left(\tilde{\mathbf{w}}_r + \tilde{\mathbf{f}}_p(\tilde{\mathbf{x}}_r, \Psi, \tilde{\mathbf{w}}) + \tilde{\mathbf{f}}_{ub}(\tau)\right) \\ \dot{\Psi} = \mathbf{g}(\tilde{\mathbf{x}}_r, \Psi, \tilde{\mathbf{w}}) \\ \dot{\tilde{\mathbf{w}}} = \frac{1}{\eta_f}\left(\frac{\tilde{\mathbf{P}}_\theta(\tilde{\mathbf{x}}_r, \Psi, \tilde{\mathbf{w}})}{\tilde{k}_b^\theta} - \tilde{\mathbf{w}}\right) \end{cases} \tag{14}$$

where $\Psi = \left[\cdots \psi_{i,j} \cdots\right]^{\mathrm{T}}$ and $\tilde{\mathbf{w}} = \left[\cdots \tilde{w}_i \cdots\right]^{\mathrm{T}}$ are the generalized coordinate vectors of the gas film and the foil structure ($i = 2, \ldots, N_\theta - 1$ and $j = 2, \ldots, N_\zeta - 1$).

For the true nature of the dynamic interaction between the rotor, the gas film, and the foil structure, the governing equations of the system are written as a set of coupled nonlinear ODEs [31]. The state vector of the coupled system is defined as:

$$\mathbf{y} = \begin{bmatrix} \tilde{\mathbf{x}}_r \\ \dot{\tilde{\mathbf{x}}}_r \\ \Psi \\ \tilde{\mathbf{w}} \end{bmatrix} \tag{15}$$

Finally, the governing equations of the entire system can be arranged in a general form as:

$$\dot{\mathbf{y}} = \mathbf{f}(\tau, \mathbf{y}) \tag{16}$$

As Eq. (16) is a stiff system, the variable-step and variable-order implicit integrator ode15s in MATLAB [42] was used for the efficient time-domain integration. At each time step, the rotor motion, the hydrodynamic pressure, and the foil deflection are solved simultaneously based on the numerical differentiation formulas (a variant of the backward differentiation formulas). The analytical Jacobian matrix $\partial \mathbf{f}/\partial \mathbf{y}$ is used to make the computation more efficient.

3 Stability analysis methods

The stability analysis of a rotor system is critical, as instability can lead to catastrophic failure. The stability analysis methods used in this work for an autonomous

GFB-rotor system, $\dot{\mathbf{y}} = \mathbf{f}(\mathbf{y})$, are revisited briefly for clarity in this section. The threshold speed for a Hopf bifurcation, which is named as the OS of instability in this paper, can be predicted by a linear stability analysis of the system's equilibrium point. Besides, nonlinear stability analysis is needed to analyze the periodic behavior before or after the OS of instability. The shooting method is adopted to find the periodic solution of the system, and then, the stability of the periodic solution can be obtained according to the Floquet theory.

3.1 Linear stability analysis

The linear stability analysis focuses on the small perturbations of the system around its equilibrium point. The equilibrium point of system (16), designated by $\mathbf{y}_s$, can be obtained by solving a set of nonlinear algebraic equations $\mathbf{f}(\mathbf{y}_s) = \mathbf{0}$ using the Newton–Raphson method. Then, the perturbation equation around the static equilibrium point can be expressed as:

$$\Delta\dot{\mathbf{y}} = \mathbf{J}(\mathbf{y}_s)\,\Delta\mathbf{y} \tag{17}$$

where the Jacobian matrix is

$$\mathbf{J}(\mathbf{y}_s) = \left.\frac{\partial\mathbf{f}(\mathbf{y})}{\partial\mathbf{y}}\right|_{\mathbf{y}=\mathbf{y}_s} \tag{18}$$

The perturbation around the static equilibrium point is assumed to be

$$\Delta\mathbf{y} = \mathbf{Y}e^{\lambda t} \tag{19}$$

Substituting Eq. (19) into Eq. (17), the corresponding standard eigenvalue problem is established as:

$$\lambda\mathbf{Y} = \mathbf{J}(\mathbf{y}_s)\,\mathbf{Y} \tag{20}$$

The eigenvalues of the Jacobian matrix determine the equilibrium point's stability property: the equilibrium point is stable if all the eigenvalues have a negative real part, while the equilibrium point is unstable if at least one of the eigenvalues has a positive real part. The Hopf bifurcation occurs where a pair of complex conjugate eigenvalues cross the imaginary axis (i.e., the real parts change sign).

3.2 Periodic solution and its stability

In this section, a solution of the system $\dot{\mathbf{y}} = \mathbf{f}(\mathbf{y})$ subject to the initial condition $\boldsymbol{\eta}$ is denoted as $\mathbf{y}(\tau;\boldsymbol{\eta})$. A solution $\mathbf{y}_p(\tau;\boldsymbol{\eta})$ is periodic if it satisfies the following conditions:

$$\dot{\mathbf{y}}_p = \mathbf{f}(\mathbf{y}_p), \quad \mathbf{y}_p(T;\boldsymbol{\eta}) = \mathbf{y}_p(0;\boldsymbol{\eta}) = \boldsymbol{\eta} \tag{21}$$

where T is the period. For a perturbation $\delta\boldsymbol{\eta}$ of initial value $\boldsymbol{\eta}$, the difference of a periodic solution $\mathbf{y}_p(\tau;\boldsymbol{\eta})$ at time T is

$$\mathbf{y}_p(T;\boldsymbol{\eta}+\delta\boldsymbol{\eta}) - \mathbf{y}_p(T;\boldsymbol{\eta}) \approx \frac{\partial\mathbf{y}_p(T;\boldsymbol{\eta})}{\partial\boldsymbol{\eta}}\delta\boldsymbol{\eta} = \mathbf{M}\delta\boldsymbol{\eta} \tag{22}$$

where $\mathbf{M} = \frac{\partial\mathbf{y}_p(T;\boldsymbol{\eta})}{\partial\boldsymbol{\eta}}$ is called the monodromy matrix. The eigenvalues of the monodromy matrix are called the Floquet multipliers and decide whether the initial perturbation decays or grows. According to the Floquet theory, the monodromy matrix has $+1$ as an eigenvalue for all periodic solutions of an autonomous system; hence, the stability of the periodic solution depends on the other eigenvalues. If all the moduli of the other eigenvalues are smaller than 1, the periodic solution is stable; otherwise, the periodic solution is unstable.

The monodromy matrix has another representation, which can be used for its calculation. The periodic solution $\mathbf{y}_p(\tau;\boldsymbol{\eta})$ satisfies the system equation; in other words, $\dot{\mathbf{y}}_p(\tau;\boldsymbol{\eta}) = \mathbf{f}(\mathbf{y}_p(\tau;\boldsymbol{\eta}))$. Taking the partial derivative of the previous equation with respect to $\boldsymbol{\eta}$ and exchanging the order of the partial differentials, a set of ODEs is obtained as follows:

$$\dot{\boldsymbol{\Phi}} = \mathbf{J}(\mathbf{y}_p)\,\boldsymbol{\Phi} \tag{23}$$

where $\boldsymbol{\Phi}(\tau) = \frac{\partial\mathbf{y}_p(\tau;\boldsymbol{\eta})}{\partial\boldsymbol{\eta}}$. At the initial moment, $\mathbf{y}(0;\boldsymbol{\eta}) = \boldsymbol{\eta}$, hence $\boldsymbol{\Phi}(0) = \frac{\partial\mathbf{y}_p(0;\boldsymbol{\eta})}{\partial\boldsymbol{\eta}} = \mathbf{I}$ where $\mathbf{I}$ is an identity matrix. Note that $\boldsymbol{\Phi}(\tau)$ depends on the periodic solution $\mathbf{y}_p$. Hence, $\boldsymbol{\Phi}(\tau)$ is called the fundamental matrix solution, which is the solution of ODE (23) with the initial condition $\boldsymbol{\Phi}(0) = \mathbf{I}$ for the periodic solution $\mathbf{y}_p$. The monodromy matrix $\mathbf{M}$ of the periodic solution $\mathbf{y}_p$ is identical to $\boldsymbol{\Phi}(T)$.

As the periodic solution of the GFB-rotor system is unknown, the shooting method is used to find a periodic solution of the system. The task is to find an initial condition $\boldsymbol{\eta}$ that leads to a periodic solution and also the corresponding period T. The shooting method starts with an initial guess for the unknown initial condition and

period; then, the initial condition and the period are corrected to fulfill the periodic condition by the Newton–Raphson iteration. The error vector corresponding to the periodic condition is defined as $\mathbf{r} = \boldsymbol{\eta} - \mathbf{y}(T; \boldsymbol{\eta})$. For an estimation $(\boldsymbol{\eta}_k, T_k)$ at the kth iteration with a correction $(\Delta\boldsymbol{\eta}_k, \Delta T_k)$, the error vector is written as:

$$\mathbf{r}_k = \boldsymbol{\eta}_k + \Delta\boldsymbol{\eta}_k - \mathbf{y}(T_k + \Delta T_k; \boldsymbol{\eta}_k + \Delta\boldsymbol{\eta}_k) \tag{24}$$

Expanding Eq. (24) into a Taylor series around $(\boldsymbol{\eta}_k, T_k)$ and truncating the series at the second term yield

$$\mathbf{r}_k \approx \boldsymbol{\eta}_k + \Delta\boldsymbol{\eta}_k - \left[\mathbf{y}(T_k; \boldsymbol{\eta}_k) + \frac{\partial \mathbf{y}}{\partial \boldsymbol{\eta}}(T_k; \boldsymbol{\eta}_k) \right.$$
$$\left. \Delta\boldsymbol{\eta}_k + \frac{\partial \mathbf{y}}{\partial T}(T_k; \boldsymbol{\eta}_k) \Delta T_k \right] \tag{25}$$

where $\mathbf{y}(\tau; \boldsymbol{\eta}_k)$ is calculated by numerically integrating $\dot{\mathbf{y}} = \mathbf{f}(\mathbf{y})$ with the initial condition $\boldsymbol{\eta}_k$, and $\frac{\partial \mathbf{y}}{\partial \boldsymbol{\eta}}(T_k; \boldsymbol{\eta}_k)$ can be found by numerically integrating (23) with $\mathbf{y}(\tau; \boldsymbol{\eta}_k)$. Furthermore, $\frac{\partial \mathbf{y}}{\partial T}(T_k; \boldsymbol{\eta}_k) = \mathbf{f}(\mathbf{y}(T_k; \boldsymbol{\eta}_k))$ is the slope of the trajectory at $\tau = T_k$.

Let error (25) be equal to zero, and then, the iterative formula for getting a better estimation is obtained as:

$$\left[\frac{\partial \mathbf{y}}{\partial \boldsymbol{\eta}}(T_k; \boldsymbol{\eta}_k) - \mathbf{I}\, \mathbf{f}(\mathbf{y}(T_k; \boldsymbol{\eta}_k)) \right] \begin{bmatrix} \Delta\boldsymbol{\eta}_k \\ \Delta T_k \end{bmatrix}$$
$$= \boldsymbol{\eta}_k - \mathbf{y}(T_k; \boldsymbol{\eta}_k) \tag{26}$$

As the number of variables is one more than the number of equations in (26), an additional orthogonality constraint $\mathbf{f}(\boldsymbol{\eta}_k) \cdot \Delta\boldsymbol{\eta}_k = 0$ is imposed, which can be approximated as $\mathbf{f}(\mathbf{y}(T_k; \boldsymbol{\eta}_k)) \cdot \Delta\boldsymbol{\eta}_k = 0$. Therefore, the complete iterative formula of the shooting method is

$$\begin{bmatrix} \frac{\partial \mathbf{y}}{\partial \boldsymbol{\eta}}(T_k; \boldsymbol{\eta}_k) - \mathbf{I}\, \mathbf{f}(\mathbf{y}(T_k; \boldsymbol{\eta}_k)) \\ \mathbf{f}^{\mathrm{T}}(\mathbf{y}(T_k; \boldsymbol{\eta}_k)) \qquad 0 \end{bmatrix} \begin{bmatrix} \Delta\boldsymbol{\eta}_k \\ \Delta T_k \end{bmatrix}$$
$$= \begin{bmatrix} \boldsymbol{\eta}_k - \mathbf{y}(T_k; \boldsymbol{\eta}_k) \\ 0 \end{bmatrix} \tag{27}$$

The solution is converged when the periodic condition is satisfied with a desired accuracy, and a periodic solution of the system is found. The monodromy matrix is also obtained as a by-product of the shooting method.

4 Results and discussions

In this section, the nonlinear dynamic characteristics of the GFB-rotor system were investigated. For all the numerical cases, the number of grid points was 150×10, and the grid independence was checked using a double-refined grid. This large number of angular points is required for simulations with a large amplitude limit cycle. The relative error tolerance of the ode15s function was set as 10^{-6}. In the simulations, the gas film height could become zero or negative due to an unstable motion or a very large amplitude motion, resulting in collisions or rubs between the rotor and the foil. This film failure would be unacceptable for an operating rotor in practice. The simulation would terminate in this case as it was beyond the capability of the present mathematical model.
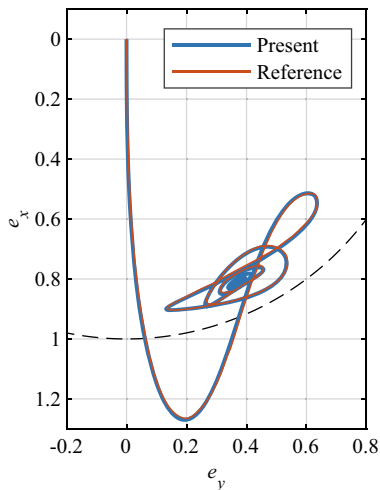
4.1 Model verification

First, the present model was verified with an experimentally validated model from Ref. [43,44]. The bearing parameters used in the numerical verification are listed in Table 1. Furthermore, the mass of the rotor was 3.06 kg with a static load of 30 N, and the rotational speed was 12,000 rpm. The rotor was released from the origin of coordinates with a zero velocity, while the initial pressure was equal to the ambient pressure, and the initial foil deflection was zero. The transient trajectories of the two simulations are illustrated in Fig. 2, where the reference data are from Ref. [44]. As can be seen, there is very good agreement between the results of the present work and Ref. [44].

4.2 Hopf bifurcation phenomena and dynamic characteristics

The Hopf bifurcation in a GFB-rotor system can be supercritical or subcritical depending on the bearing

Table 1 The parameters of the GFB

Parameters	Value
Bearing radius, R	19.05 mm
Bearing length, L	38.1 mm
Bearing clearance, C	31.8 μm
Foil structural stiffness, k_b	4.6417 GN/m^3
Foil structural loss factor, η_f	0.25
Ambient pressure, p_a	1.01325×10^5 Pa
Dynamic viscosity, μ	1.95×10^{-5} Ns/m^2

Fig. 2 Comparison of the two transient trajectories for numerical verification

parameters. This section aims to give a complete characterization of these two bifurcation phenomena and their dynamic characteristics.

In order to highlight the influence of the bearing design on the nonlinear characteristics for a given rotor system, the aspect ratio L/D (where $D = 2R$ is the bearing diameter), the foil structural stiffness k_b, and the loss factor η_f were chosen as the design parameters. The different sets of design parameters would lead to different types of Hopf bifurcations. Furthermore, the other bearing parameters were held constant as listed in Table 1. The mass of the rotor was set as 2.04 kg, and the static load was 20 N. To focus on the inherent attributes of the system, the unbalance u was set as 0 in Sects. 4.2.1 and 4.2.2.

4.2.1 Supercritical and subcritical Hopf bifurcation phenomena

With a typical set of design parameters, $L/D = 2$, $k_b = 5 \times 10^9$ N/m^3, and $\eta_f = 0.25$, the system undergoes a supercritical Hopf bifurcation. The OS of instability (i.e., the bifurcation point) is 11,475 rpm. The equilibrium solution and the periodic solution (if it existed) were obtained for different rotational speeds, and their stabilities were evaluated using the methods given in Sect. 3. The bifurcation diagram is illustrated in Fig. 3a, where the stable solutions are indicated by solid lines, and the unstable solutions are indicated by dashed lines. The equilibrium and periodic solutions at

13,000 rpm are plotted in Fig. 3b, and the Floquet multipliers of the periodic solution are plotted in Fig. 3c. It is clear to see that as the speed exceeds the OS of instability, a branch of stable equilibrium solutions bifurcates into a branch of unstable equilibrium solutions and a branch of stable periodic solutions. However, because a large amplitude periodic solution leads to the film failure, there is an upper limit for the speed accompanied by a stable periodic solution. The existence of stable periodic solutions indicates that the machine may still operate even if the speed exceeds the OS of instability for a well-balanced rotor or for other cases where a small oscillation in the narrow clearance of the gas bearing is acceptable [15].

On the other side, the system undergoes a subcritical Hopf bifurcation with the design parameters of $L/D = 1$, $k_b = 5 \times 10^9$ N/m^3, and $\eta_f = 0.25$, as shown in Fig. 4. The OS of instability (i.e., the bifurcation point) is 17,367 rpm. Different from the supercritical Hopf bifurcation, when the speed decreases and passes through the OS of instability, the subcritical Hopf bifurcation has a branch of unstable equilibrium solutions bifurcating into a branch of stable equilibrium solutions and a branch of unstable periodic solutions. Again, there is a minimum speed for the existence of the unstable periodic solutions, because of the film failure. Note that for this subcritical case, no stable solution can be obtained once the speed exceeds the bifurcation point, which means a sudden and unpredictable failure of the bearing.

4.2.2 Shock stability characteristics

The shock stability characteristics of a system with a supercritical or a subcritical Hopf bifurcation were studied. The shock stability discussed here refers to the ability of the system to resume stable operation after suffering nondestructive shocks with a rotational speed lower than the OS of instability. The responses after the end of shocks were concerned, and the effects of the shocks were equivalent to various initial conditions that are dominated by the rotor position. That is, the rotor was initially constrained to a given position with zero velocity, and the initial film pressure and foil deflection were computed under the condition that the gas film force, the static load, and the constrained force were balanced. Then, the dynamic simulation was started with releasing the rotor by removing the constrained force. The initial dimensionless rotor position
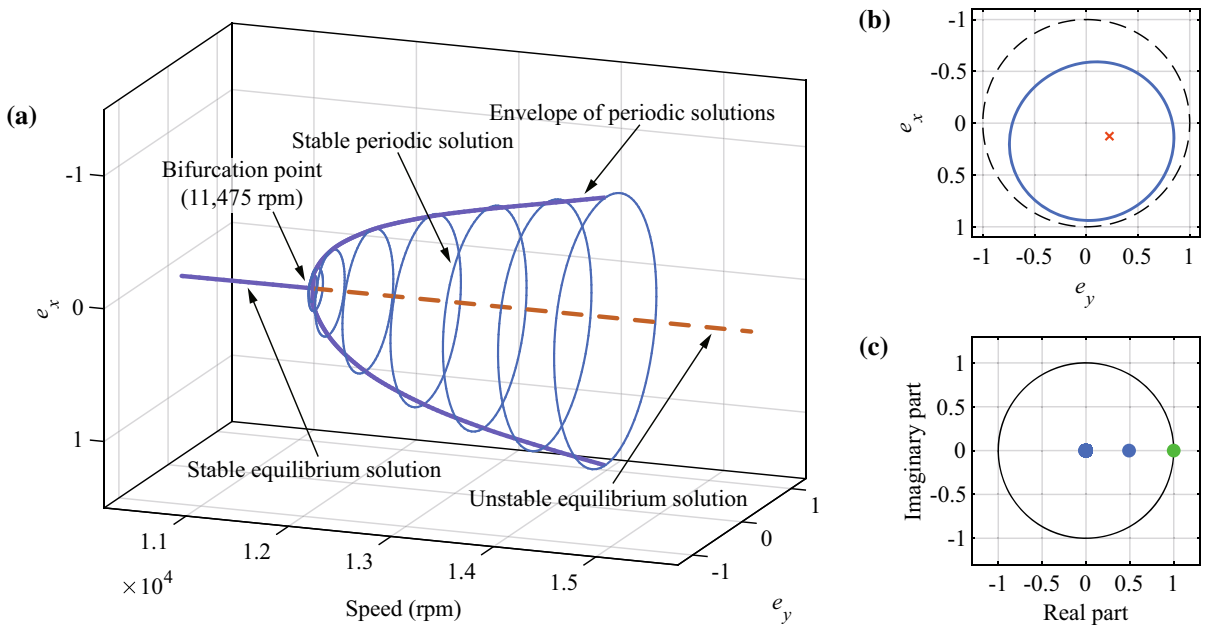
Fig. 3 Supercritical Hopf bifurcation with $L/D = 2$, $k_b = 5 \times 10^9$ N/m^3, and $\eta_f = 0.25$: **a** bifurcation diagram, **b** equilibrium solution and periodic solution at 13,000 rpm, and **c** Floquet multipliers of the periodic solution at 13,000 rpm
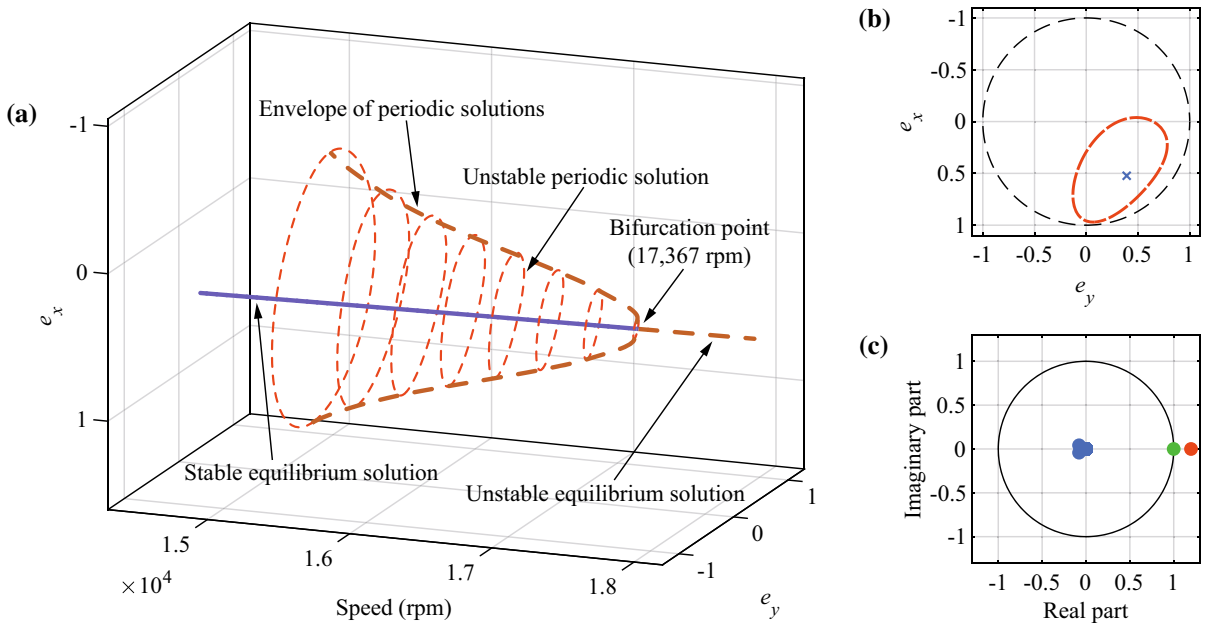
Fig. 4 Subcritical Hopf bifurcation with $L/D = 1$, $k_b = 5 \times 10^9$ N/m^3, and $\eta_f = 0.25$: **a** bifurcation diagram, **b** equilibrium solution and periodic solution at 16,000 rpm, and **c** Floquet multipliers of the periodic solution at 16,000 rpm

was limited within the unit circle, which means a non-destructive shock.

For a system with a supercritical Hopf bifurcation, the rotor could always converge to the equilibrium point after nondestructive shocks in the simulations. It suggests that there is no shock stability problem for this type of system.

For a system with a subcritical Hopf bifurcation, the convergence of the rotor trajectory depends on the magnitude of the shock as an unstable periodic solution exists. The initial position that makes the rotor converge to the equilibrium point belongs to the basin of attraction of the static equilibrium point. The case with the design parameters of $L/D = 1$, $k_b = 5 \times 10^9$ N/m^3, and $\eta_f = 0.25$ was used as an example, whose OS of instability is 17,367 rpm. The boundaries of the basins of attraction at various speeds are plotted in Fig. 5a. Two trajectories of the rotor with a small difference of initial positions near the asterisks in Fig. 5a inside and outside the basin of attraction at 16,000 rpm are given in Fig. 5b and c. As can be seen, along with the increase in the speed, the size of the basin of attraction decreases and becomes nearly zero at the OS of instability. Hence, for a rotor system with a subcritical Hopf bifurcation, the actual available speed may be far lower than the OS of instability when considering the shock stability. It should be explained that, for some cases with a subcritical Hopf bifurcation, the divergent trajectory can converge to a stable periodic solution outside the unstable periodic solution. This stable periodic solution does not lead to the film failure but usually has a large amplitude. Moreover, it can be observed only near the transition point of the two bifurcation types, which is discussed in detail in Sect. 4.3.
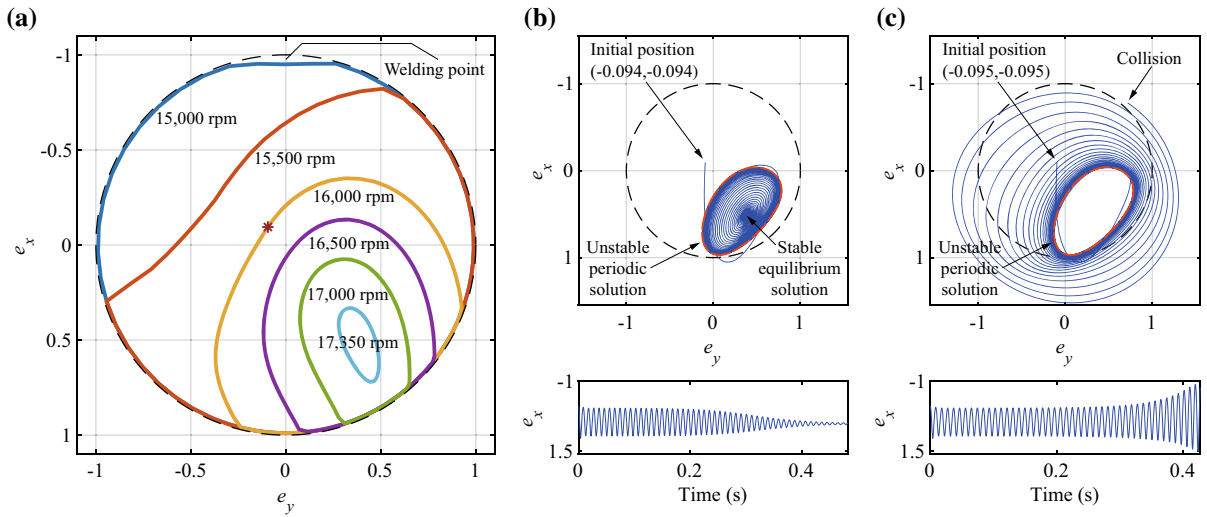
4.2.3 Unbalanced response characteristics

The unbalanced response characteristics of a system with a supercritical or a subcritical Hopf bifurcation were investigated. In order to study the steady-state response of the rotor under unbalanced excitation, the time-domain simulation was started from the equilibrium state obtained without an unbalance and was ended when the trajectory was stable for a sufficiently long time, where the magnitude of the unbalance u was calculated based on the ISO balance grade and the OS of instability.

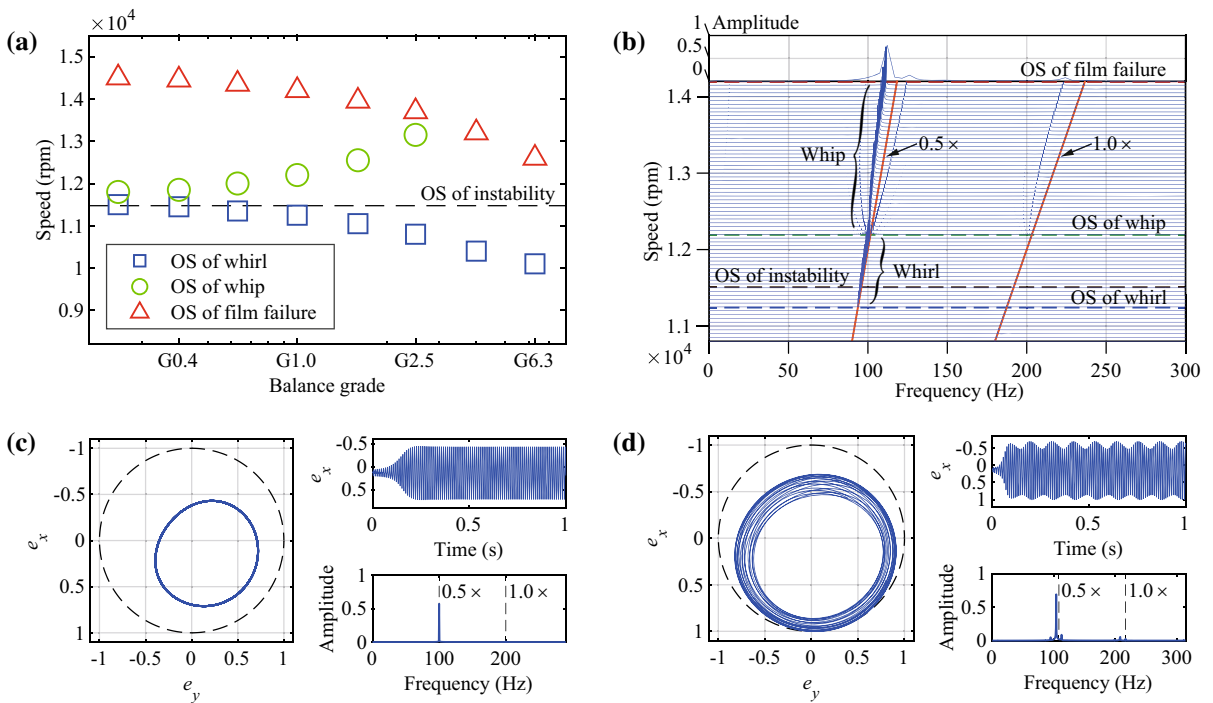The case of a supercritical Hopf bifurcation was first studied with the design parameters of $L/D = 2$,

$k_b = 5 \times 10^9$ N/m^3, and $\eta_f = 0.25$. Two typical sub-synchronous vibration phenomena were observed (i.e., whirl and whip motions). A whirl motion is dominated by the unbalanced force, and its frequency is equal to half of the rotational speed, while a whip motion is dominated by the self-excited effect of the gas film. Figure 6a gives a complete description of the changes in the OS of the whirl, whip, and film failure with different balance grades. The waterfall diagram under a balance grade of G1.0 is plotted in Fig. 6b. The steady-state trajectory, the transient curve, and the FFT diagram at the speeds of 12,000 rpm and 13,000 rpm under a balance grade of G1.0 are given in Fig. 6c and d to characterize the whirl and whip motions, respectively. The whirl motion appears first as a forced nonlinear vibration with the increase in the rotational speed. The whip motion does not immediately appear when the speed exceeds the OS of instability, where the frequency of the self-excited vibration becomes synchronized with the half frequency of the unbalanced excitation. With the further increase in the rotational speed, the amplitude of the self-excited vibration increases, and the frequency-locking disappears, resulting in a beat vibration because the self-excited frequency is close to half the rotational speed. With the increase in the unbalance, the OS of the whirl and film failure shows a downward trend while the OS of the whip motion shows an upward trend, which agrees with the result of Ref. [10]. Under low balance grades, the reason for the film failure is the excessive amplitude of the whip motion; under a balance grade larger than G2.5, the film fails due to the excessive amplitude of the whirl motion, and the whip motion disappears, which can explain the result of Ref. [15]. The gas film can still work without failure at a speed higher than the OS of instability even under a balance grade of G6.3, indicating a good unbalance tolerance for the system with a supercritical Hopf bifurcation.

For the case of a subcritical Hopf bifurcation with the design parameters of $L/D = 1$, $k_b = 5 \times 10^9$ N/m^3, and $\eta_f = 0.25$, the unbalanced response characteristics are shown in Fig. 7. It is clear to see that, compared to the case with a supercritical Hopf bifurcation, the unbalanced response characteristics of the subcritical Hopf bifurcation are much simpler. No subsynchronous vibration is found within the studied parameter range. The OS of the film failure is lower than the OS of instability and decreases rapidly with the increase in the balance grade. This can be intuitively understood by the
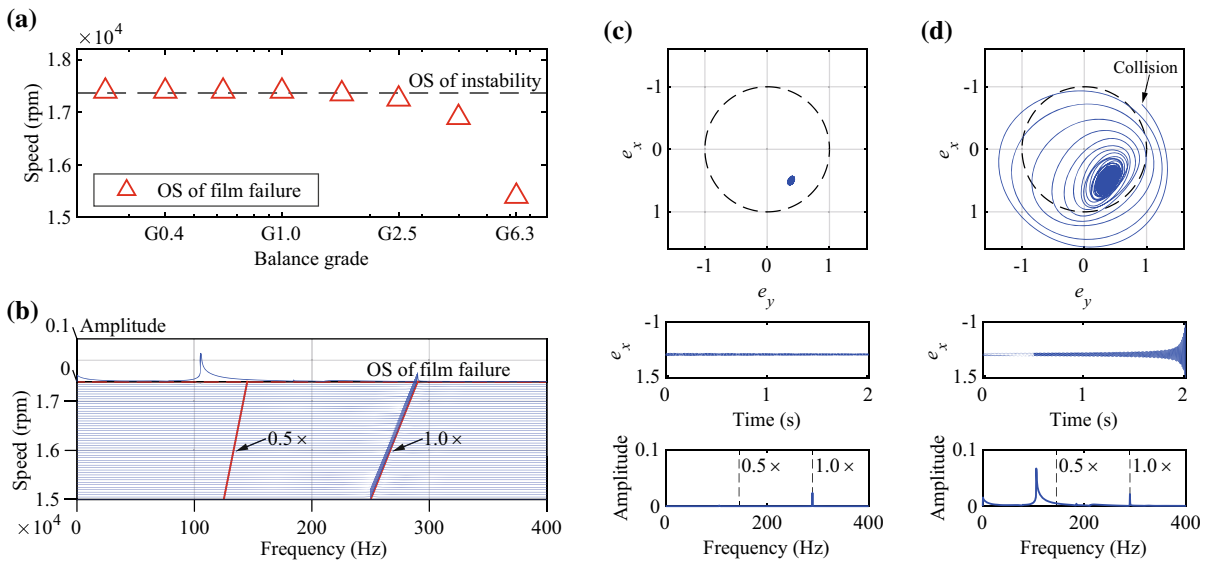
Fig. 5 Shock stability characteristics of a subcritical Hopf bifurcation with $L/D = 1$, $k_b = 5 \times 10^9$ N/m³, and $\eta_f = 0.25$: **a** the boundaries of the basins of attraction at various speeds, **b** convergent trajectory, and **c** divergent trajectory with a small difference of initial positions at 16,000 rpm

Fig. 6 Unbalanced response characteristics of a supercritical Hopf bifurcation with $L/D = 2$, $k_b = 5 \times 10^9$ N/m³, and $\eta_f = 0.25$: **a** complete description of the changes in the OS of the whirl, whip, and film failure with the balance grade, **b** waterfall diagram under a balance grade of G1.0, **c** whirl at 12,000 rpm under a balance grade of G1.0, and **d** whip at 13,000 rpm under a balance grade of G1.0

(a)

(b)

(c)

(d)

Fig. 7 Unbalanced response characteristics of a subcritical Hopf bifurcation with $L/D = 1$, $k_b = 5 \times 10^9$ N/m^3, and $\eta_f = 0.25$: **a** complete description of the change in the OS of the film failure with the balance grade, **b** waterfall diagram under a balance

grade of G1.0, **c** transient response at 17,350 rpm under a balance grade of G1.0, and **d** transient response at 17,400 rpm under a balance grade of G1.0

boundaries of the basins of attraction shown in Fig. 5a. A large unbalance leads to a large deviation from the equilibrium point, while the basin of attraction narrows as the rotational speed increases. Hence, for a system with a subcritical Hopf bifurcation, the actual available speed is also lower than the OS of instability under a large unbalance.

4.3 Parameter study

According to the analysis presented in Sect. 4.2, the available speed for a GFB-rotor system may be much lower than the OS of instability, due to the poor dynamic characteristics of the subcritical Hopf bifurcation. The parameter design of a GFB has a significant influence on the Hopf bifurcation type and thus the nonlinear characteristics of the system. In this section, the influences of the bearing parameters on the nonlinear characteristics and the available speed of a well-balanced GFB-rotor system were investigated. For ease of expression and understanding, two speed limits are defined here as follows:

(1) *Actual speed limit*. When operating below this speed, the rotor can always return to the stable equilibrium point after suffering any nondestructive shock.

(2) *Ideal speed limit*. When operating below this speed, the rotor returns to the stable equilibrium point or a stable periodic solution after suffering any nondestructive shock.

These two speed limits were obtained by the nonlinear time-domain simulations. Based on the definitions, the actual speed limit is the upper limit of the operating speed applicable to all devices, while the ideal speed limit can only serve as a reference for devices tolerating small oscillations. However, the speed range between the two speed limits characterizes the existence of stable periodic solutions, so these two speed limits are both considered in this section for a complete description of change in bifurcation behaviors.
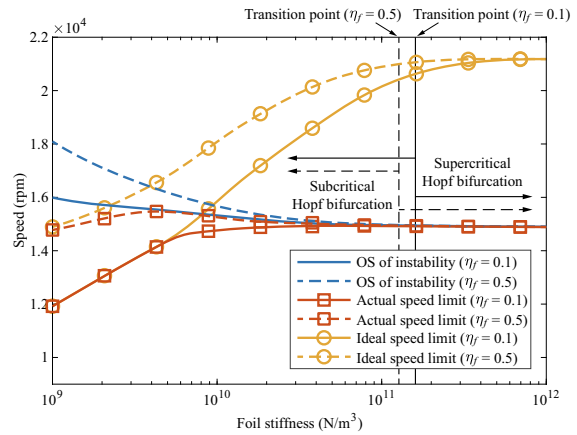
The influence of the aspect ratio L/D on the OS of instability and the two speed limits was first investigated as illustrated in Fig. 8 with $k_b = 5 \times 10^9$ N/m^3 and $\eta_f = 0.25$, where the corresponding bifurcation diagrams are also attached for a better understanding. It can be seen that all three curves show a downward trend with the increase in the aspect ratio, and the actual speed limit is significantly less sensitive than the OS of instability. The differences between the three curves come from the change of Hopf bifurcation behaviors. For a low aspect ratio, the subcritical Hopf bifurcation occurs
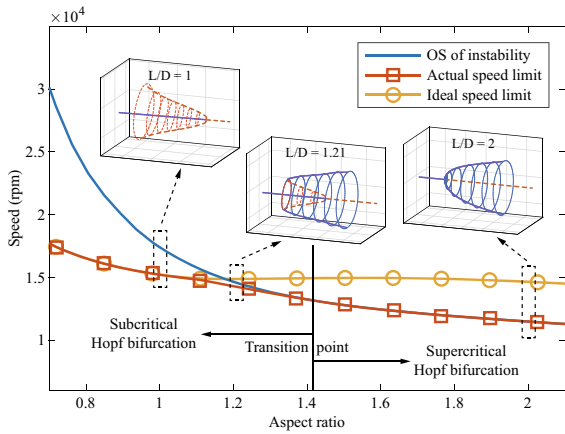
Fig. 8 Influence of the aspect ratio L/D on the OS of instability and the two speed limits with $k_b = 5 \times 10^9$ N/m^3 and $\eta_f = 0.25$


Fig. 9 Influence of the foil structural stiffness k_b and the loss factor η_f on the OS of instability and the two speed limits with $L/D = 1.1$

and leads to a considerable range of unavailable speed below the OS of instability. With the increase in the aspect ratio, the subcritical Hopf bifurcation changes into the supercritical Hopf bifurcation and results in an extension of the ideal speed limit. Note that near the transition point of the two bifurcations, a global bifurcation can still occur which indicates that a stable equilibrium solution, an unstable periodic solution, and a stable periodic solution coexist within the physical boundary, as mentioned in Sect. 4.2.2. This situation can be treated directly as a supercritical Hopf bifurcation with a reduced OS of instability when it comes to its nonlinear characteristics, although it is actually a subcritical Hopf bifurcation at the bifurcation point according to the definition of local bifurcation. Besides, the decrease in the aspect ratio under a fixed bearing diameter can be viewed as an increase in the static load. So, it can be said that the supercritical Hopf bifurcation changes into the subcritical Hopf bifurcation with the increase in the static load. This agrees with the result of Ref. [9] that the increase in the static load leads to a decrease and finally a disappearance of the subsynchronous vibrations under unbalanced excitation.

Similarly, Fig. 9 gives the influence of the foil structural stiffness k_b and the loss factor η_f on the OS of instability and the two speed limits with $L/D = 1.1$. For the foil stiffness, the linear results are consistent with Ref. [7,11,13] (i.e., the flexibility of the foil structure can improve the OS of instability). However, the nonlinear results have shown almost completely opposite conclusions. The improvement of the OS of insta-

bility arising from a softer foil structure is offset by the transition from a supercritical Hopf bifurcation to a subcritical Hopf bifurcation. The good news is that the increase in the foil structural loss factor can significantly improve both the linear and nonlinear results at a low foil stiffness, which means the effectiveness of a soft foil structure to increase the actual speed limit depends on the damping characteristics of the foil structure. Therefore, if there is no sufficient damping in the structure, a higher foil stiffness should be the first choice considering the actual available speed, thanks to the excellent shock stability and unbalanced response characteristics of the supercritical Hopf bifurcation compared to the subcritical one. Besides, the results can give an excellent explanation to the existence of stable periodic solutions along with the change of the foil structural stiffness found in Ref. [30,31].

A comprehensive view of the effect of the design parameters on the Hopf bifurcation type and the relative difference between the OS of instability and the actual speed limit is given in Fig. 10. As can be seen, for a lower foil stiffness, a larger aspect ratio is needed to have a supercritical Hopf bifurcation behavior. The loss factor has a relatively small effect on the Hopf bifurcation type. For a system with a supercritical Hopf bifurcation, the OS of instability and the actual speed limit are in agreement (i.e., the relative difference is zero), while for a system with a subcritical Hopf bifurcation, the relative difference increases when moving away from the transition line.
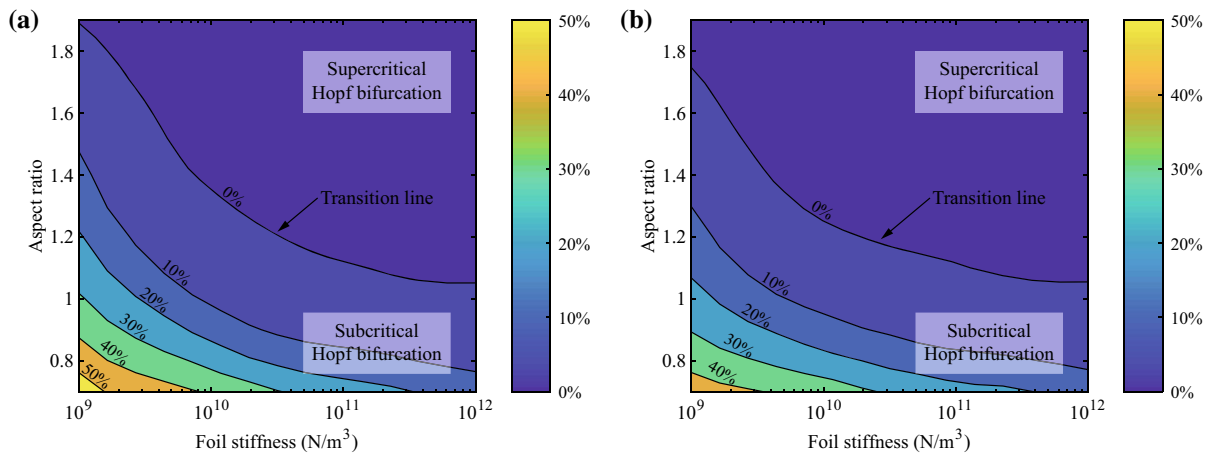
Fig. 10 The relative difference between the OS of instability and the actual speed limit: **a** $\eta_f = 0.1$ and **b** $\eta_f = 0.5$

5 Conclusions

The nonlinear dynamic characteristics of GFB-rotor systems with a supercritical or a subcritical Hopf bifurcation have been presented in this paper. The governing equation of the fully coupled system was established to simultaneously solve the rotor motion, the hydrodynamic pressure, and the foil deflection. The OS of instability (i.e., the bifurcation point) was predicted by the linear stability analysis. The periodic solution of the system before or after the bifurcation point was obtained by the shooting method, and its stability was assessed by the Floquet multipliers.

The shock stability and unbalanced response characteristics of the two Hopf bifurcation types were investigated, and the results reveal that the subcritical Hopf bifurcation is far more dangerous than the supercritical one. For a system with a supercritical Hopf bifurcation, when operating below the OS of instability, the rotor can always return to stable operation after experiencing any nondestructive shock. With unbalanced excitation, whirl and whip motions were both observed, and the bearing could still work without failure when operating above the OS of instability. For a system with a subcritical Hopf bifurcation, even operating at a speed below the OS of instability, the rotor may diverge and contact with the foil structure after experiencing a nondestructive shock. With unbalanced excitation, whirl and whip motions did not appear, and the film would fail suddenly as the speed increases to a threshold speed lower than the OS of instability. Hence, for a practical GFB-rotor system that lacks Hopf bifurcation analysis during the design stage, the system may undergo a subcritical Hopf bifurcation and suffer an unpredictable failure even operating at a speed below the OS of instability.

A parameter analysis of the aspect ratio, the foil stiffness, and the loss factor on the Hopf bifurcation type and the actual speed limit was carried out, and significant differences were observed between the nonlinear results and the linear results. The aspect ratio and the foil stiffness have obvious effects on the Hopf bifurcation type of the system, while the loss factor has a relatively small effect. For the actual speed limit, all three parameters have obvious effects. As the aspect ratio increases, both the OS of instability and the actual speed limit decrease. A lower foil stiffness can increase the OS of instability; however, the actual speed limit would probably decrease as the Hopf bifurcation changes from a supercritical type to a subcritical type. With a low foil stiffness, a large loss factor is an obvious improvement for the actual speed limit as well as the OS of instability.

Therefore, to avoid the undesired subcritical Hopf bifurcation in a practical GFB-rotor system, the investigation on the Hopf bifurcation type and actual available speed based on nonlinear dynamic analysis is of great necessity during the bearing design stage.

Availability of data and material All data generated during the study are available from the corresponding author by request.

Compliance with ethical standards

Conflict of interest The authors declare that they have no conflict of interest or competing interest with regard to the publication of this manuscript.

Code availability Custom code.

References

1. Agrawal, G.L.: Foil air/gas bearing technology-an overview, In: ASME 1997 International Gas Turbine and Aeroengine Congress and Exhibition, American Society of Mechanical Engineers Digital Collection, pp. 1–11(1997)

2. Samanta, P., Murmu, N., Khonsari, M.: The evolution of foil bearing technology. Tribol. Int. **135**, 305–323 (2019)

3. DellaCorte, C.: Oil-Free shaft support system rotordynamics: Past, present and future challenges and opportunities. Mech. Syst. Signal Process. **29**, 67–76 (2012)

4. Heshmat, H.: Advancements in the performance of aerodynamic foil journal bearings: High speed and load capability. J. Tribol. **116**(2), 287–294 (1994). https://doi.org/10.1115/1.2927211

5. Lund, J.W.: Calculation of stiffness and damping properties of gas bearings. J. Lubr. Technol. **90**(4), 793–803 (1968). https://doi.org/10.1115/1.3601723

6. Peng, J.-P., Carpino, M.: Calculation of stiffness and damping coefficients for elastically supported gas foil bearings. J. Tribol. **115**(1), 20–27 (1993). https://doi.org/10.1115/1.2920982

7. Vleugels, P., Waumans, T., Peirs, J., Al-Bender, F., Reynaerts, D.: High-speed bearings for micro gas turbines: Stability analysis of foil bearings. J. Micromech. Microeng. **16**(9), S282 (2006)

8. Kim, D.: Parametric studies on static and dynamic performance of air foil bearings with different top foil geometries and bump stiffness distributions. J. Tribol. **129**(2), 354–364 (2006). https://doi.org/10.1115/1.2540065

9. Hoffmann, R., Pronobis, T., Liebich, R.: Non-linear stability analysis of a modified gas foil bearing structure, In: Proceedings of the 9th IFToMM International Conference on Rotor Dynamics, Springer, pp. 1259–1276 (2015)

10. Hoffmann, R., Liebich, R.: Characterisation and calculation of nonlinear vibrations in gas foil bearing systems-An experimental and numerical investigation. J. Sound Vib. **412**, 389–409 (2018)

11. Larsen, J.S., Santos, I.F., von Osmanski, S.: Stability of rigid rotors supported by air foil bearings: Comparison of two fundamental approaches. J. Sound Vib. **381**, 179–191 (2016)

12. Pronobis, T., Liebich, R.: Comparison of stability limits obtained by time integration and perturbation approach for Gas Foil Bearings. J. Sound Vib. **458**, 497–509 (2019)

13. von Osmanski, S., Larsen, J.S., Santos, I.F.: Multi-domain stability and modal analysis applied to gas foil bearings: Three approaches. J. Sound Vib. **472**, 115174 (2020)

14. Bonello, P.: The extraction of Campbell diagrams from the dynamical system representation of a foil-air bearing rotor model. Mech. Syst. Signal Process. **129**, 502–530 (2019)

15. San Andrés, L., Kim, T.H.: Forced nonlinear response of gas foil bearing supported rotors. Tribol. Int. **41**(8), 704–715 (2008)

16. Bhore, S.P., Darpe, A.K.: Nonlinear dynamics of flexible rotor supported on the gas foil journal bearings. J. Sound Vib. **332**(20), 5135–5150 (2013)

17. Balducchi, F., Arghir, M., Gaudillere, M.: Experimental analysis of the unbalance response of rigid rotors supported on aerodynamic foil bearings, In: ASME Turbo Expo 2014: Turbine Technical Conference and Exposition, American Society of Mechanical Engineers Digital Collection, V07BT32A009 (2014)

18. Larsen, J.S., Santos, I.F.: On the nonlinear steady-state response of rigid rotors supported by air foil bearings-theory and experiments. J. Sound Vib. **346**, 284–297 (2015)

19. Bonello, P., Pham, H.M.: Nonlinear dynamic analysis of high speed oil-free turbomachinery with focus on stability and self-excited vibration. J. Tribol. **136**(4), 216–223 (2014a)

20. Wang, C.-C., Chen, C.-K.: Bifurcation analysis of self-acting gas journal bearings. J. Trib. **123**(4), 755–767 (2001)

21. Wang, C.-C.: Application of a hybrid numerical method to the nonlinear dynamic analysis of a micro gas bearing system. Nonlinear Dyn. **59**(4), 695–710 (2010)

22. Zhang, J., Kang, W., Liu, Y.: Numerical method and bifurcation analysis of Jeffcott rotor system supported in gas journal bearings, J. Comput. Nonlinear Dynam. **4**(1)

23. Lu, Y., Zhang, Y., Shi, X., Wang, W., Yu, L.: Nonlinear dynamic analysis of a rotor system with fixed-tilting-pad self-acting gas-lubricated bearings support. Nonlinear Dyn. **69**(3), 877–890 (2012)

24. Zhang, X.-Q., Wang, X.-L., Zhang, Y.-Y.: Non-linear dynamic analysis of the ultra-short micro gas journal bearing-rotor systems considering viscous friction effects. Nonlinear Dyn. **73**(1–2), 751–765 (2013)

25. Zhang, G.-H., Sun, Y., Liu, Z.-S., Zhang, M., Yan, J.-J.: Dynamic characteristics of self-acting gas bearing-flexible rotor coupling system based on the forecasting orbit method. Nonlinear Dyn. **69**(1–2), 341–355 (2012)

26. Rashidi, R., et al.: Preload effect on nonlinear dynamic behavior of a rigid rotor supported by noncircular gas-lubricated journal bearing systems. Nonlinear Dyn. **60**(3), 231–253 (2010)

27. Liu, W., Feng, K., Lyu, P.: Bifurcation and nonlinear dynamic behaviours of a metal mesh damped flexible pivot tilting pad gas bearing system. Nonlinear Dyn. **91**(1), 655–677 (2018)

28. Brancati, R., Russo, M., Russo, R.: On the stability of periodic motions of an unbalanced rigid rotor on lubricated journal bearings. Nonlinear Dyn. **10**(2), 175–185 (1996)

29. Gu, Y., Ma, Y., Ren, G.: Stability and vibration characteristics of a rotor-gas foil bearings system with high-static-low-dynamic-stiffness supports. J. Sound Vib. **397**, 152–170 (2017)

30. Pham, H., Bonello, P.: Efficient techniques for the computation of the nonlinear dynamics of a foil-air bearing rotor system, In: ASME Turbo Expo 2013: Turbine Technical Con-

ference and Exposition, American Society of Mechanical Engineers Digital Collection, V07BT30A011 (2013)

31. Bonello, P., Pham, H.: The efficient computation of the non-linear dynamic response of a foil-air bearing rotor system. J. Sound Vib. **333**(15), 3459–3478 (2014)

32. Yang, P., Zhu, K.-Q., Wang, X.-L.: On the non-linear stability of self-acting gas journal bearings. Tribol. Int. **42**(1), 71–76 (2009)

33. Seydel, R.: Practical Bifurcation and Stability Analysis, vol. 5. Springer Science & Business Media, Berlin (2009)

34. Myers, C.J.: Bifurcation theory applied to oil whirl in plain cylindrical journal bearings. J. Appl. Mech. **51**(2), 244–250 (1984). https://doi.org/10.1115/1.3167607

35. Hollis, P., Taylor, D.: Hopf bifurcation to limit cycles in fluid film bearings. J. Tribol. **108**(2), 184–189 (1986). https://doi.org/10.1115/1.3261158

36. Wang, J., Khonsari, M.: Bifurcation analysis of a flexible rotor supported by two fluid-film journal bearings. J. Tribol. **128**(3), 594–603 (2006). https://doi.org/10.1115/1.2197842

37. Chouchane, M., Amamou, A.: Bifurcation of limit cycles in fluid film bearings. Int. J. Non-Linear Mech. **46**(9), 1258–1264 (2011)

38. Chasalevris, A.: Stability and Hopf bifurcations in rotor-bearing-foundation systems of turbines and generators. Tribol. Int. **145**, 106154 (2020)

39. Hamrock, B.J., Schmid, S.R., Jacobson, B.O.: Fundamentals of Fluid Film Lubrication. CRC Press, USA (2004)

40. Heshmat, H., Walowit, J., Pinkus, O.: Analysis of gas-lubricated foil journal bearings. Asme J. Lubr. Technol **105**(4), 647 (1983)

41. Kim, T.H., San Andrés, L.: Heavily loaded gas foil bearings: a model anchored to test data. J. Eng. Gas Turbines Power **130**(1), 82–93 (2008)

42. Shampine, L.F., Reichelt, M.W.: The MATLAB ODE Suite. SIAM J. Sci. Comput. **18**(1), 1–22 (1997)

43. Larsen, J.S.: Nonlinear analysis of rotors Supported by air foil journal bearings–theory and experiments, DTU Mechanical Engineering (2014)

44. Nielsen, B.B., Santos, I.F.: Transient and steady state behaviour of elasto-aerodynamic air foil bearings, considering bump foil compliance and top foil inertia and flexibility: A numerical investigation. Proc. Inst. Mech. Eng., Part J: J. Eng. Tribol. **231**(10), 1235–1253 (2017)